Measurement 270 (2026) 120932

Contents lists available at ScienceDirect

Measurement

journal homepage: www.elsevier.com/locate/measurement

Measurement of a tyre's inner liner point dynamics with pose estimation

Emanuele Zappa [a], Luca Parenzan [a], Edoardo Montini [a,*], Stefano Melzi [a], Andrea Gregorini [a], Andrea Natta [b]

[a] Politecnico di Milano, Mechanical Engineering Department, Via La Masa 1, 20156 Milano, Italy
[b] Pirelli Tyre S.p.A., Viale Piero e Alberto Pirelli 25, 20156 Milano, Italy

ARTICLE INFO

Keywords:
Pose Estimation
Tyre Dynamics
Displacement and Rotation analysis
Optical Measurement
Controlled testing environment

ABSTRACT

The objective of this study was to design a measurement system device for investigating the dynamics of a rolling tire under controlled conditions by estimating the 3D motion of a rigid target mounted on the tire's inner liner. Tire dynamics is a critical and rapidly advancing area in the automotive industry. To address this challenge, the project aimed to develop a system that utilizes a compact action camera connected to the rim to accurately measure the behavior of the tire's inner liner with minimal uncertainty. The adopted measuring technique is pose estimation, which allows for estimating the displacement and rotation of a rigid target using single-camera images. To validate the proposed method, experiments were conducted on a flat track machine at the Pirelli Tyre S.p.A. testing facility. This specialized equipment simulates tire-road interactions, providing a controlled setting where each test condition is associated with well-defined, constant parameters. This setup allowed careful validation and reliable performance comparisons across various test scenarios.

1. Introduction

The tyre contact patch is a critical area where the interaction forces between a vehicle and the road are exchanged. Understanding the dynamics of this region, both in terms of displacement and deformation, is essential for improving tyre modelling, numerical parametrization, and validation.

Researchers have developed various techniques over the years to measure tyre displacement during operation. Early solutions included the Darmstadt tyre sensor, which used a magnetic sensor to measure tread displacement [1]. Other methods discussed in literature involve LEDs placed on the tyre [2], or laser triangulation [3]. Recently, there has been significant interest in accelerometers placed on the tyre's internal surface, enabling the acquisition of accelerometric signals and the integration of associated displacements [4]. However, these techniques typically measure displacements of the target point, but they do not capture the complete movement, since do not allow to estimate the rotation. Moreover, accelerometer-based techniques need a double numerical integration to obtain the displacements, with severe increase of the measuring uncertainty. Previous cited articles have limitation either in terms of system integration, where there is the need of a physical sensor to be mounted on the analysed mechanical system, or in terms of limited reconstructed degrees of freedom.

References [5] and [6] investigate tyre deformation using two distinct methodologies. The former employs Digital Image Correlation (DIC), utilizing multiple viewpoints of a speckle pattern applied to the tyre's inner liner. In contrast, the latter uses strain gauges to directly measure deformation on the inner liner surface.

Reference [7] adopts a different approach by tracking the displacement of a limited number of points, which can be measured in either 2D or 3D depending on the experimental setup. The applied load is inferred from the deformation of this point grid. A camera mounted on the rim captures the data, with the primary objective of reconstructing the load. However, the system does not provide full 3D displacement fields; instead, it estimates force based on the observed point displacements.

In [8], time-of-flight measurements are used to evaluate the radial deflection of the tyre carcass. This method does not yield information about lateral or longitudinal displacements. Additionally, radial measurements may be affected by deformations in these directions, potentially causing shifts in the reference point on the inner liner and increasing the overall uncertainty.

Finally, references [9] and [10] explore tyre dynamics reconstruction using camera-based systems. The former captures images from outside the tyre, offering no insight into inner liner motion or deformation. The latter observes from within the tyre but is limited to low-speed applications due to the need for rim modification. Moreover,

* Corresponding author.
E-mail address: edoardo.montini@polimi.it (E. Montini).

https://doi.org/10.1016/j.measurement.2026.120932
Received 4 April 2025; Received in revised form 21 January 2026; Accepted 22 February 2026
Available online 23 February 2026

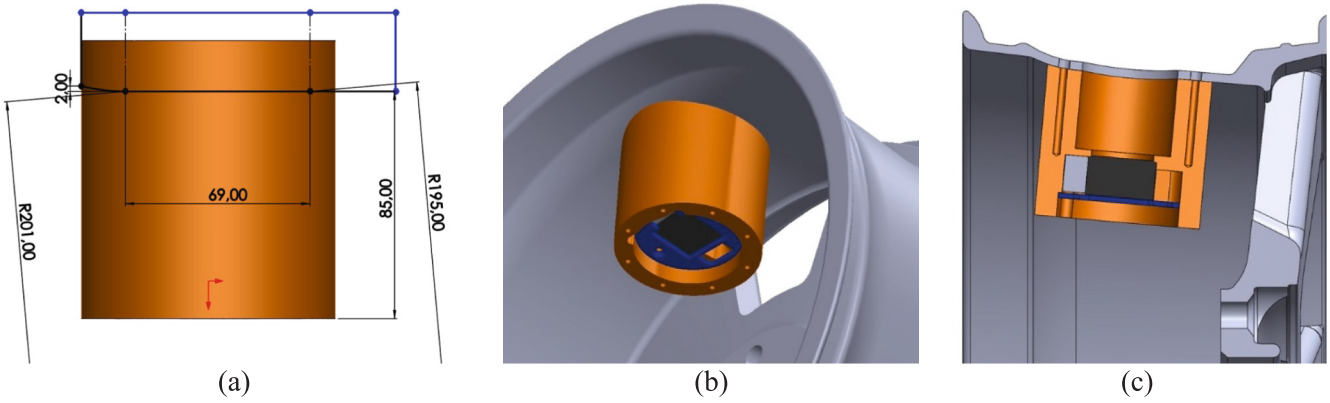

Fig. 1. Camera support simulation mounting: revolved cut of support (a), side view of the support fastened (b), section view of the support fastened (c).

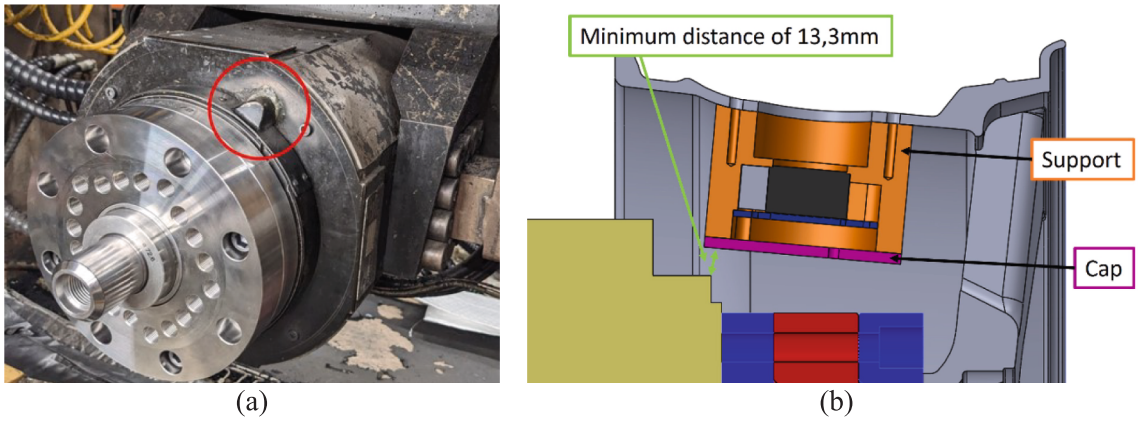

Fig. 2. Flat track most critical section (a), final configuration of the support mounted on the rim and mounted on the flat track (b).

since the camera does not rotate with the tyre, it only captures the contact patch region.

The work presented in this article focuses on the displacement reconstruction of a rigid body by means of a single camera installed within the rim and adopting the pose estimation technique. The usage of this type of technique can be done in different ways. [11] uses event-camera in space application, detecting when a condition is changing. [12], instead, highlights how the pose estimation can be used to understand the position of two cameras starting from a single frame. [13,14] highlight the power of pose estimation to fully understand structural vibration and movements, avoiding collision and without putting in contact acquisition system that might cause a variation in the dynamic performances of the analysed system. Pose estimation involves estimating an object's 6 degrees of freedom given camera intrinsic parameters, and correspondences between 3D reference points of the target and their 2D images. Known as the Perspective-n-Point (PnP) problem, it was first proposed by Fischler and Bolles in 1981 [15]. While closed-form solutions exist for configurations like three and four feature points, they are idealized and may not be reliable under real-world conditions [16,17]. Iterative methods, such as nonlinear least squares optimization, are often preferred for robust pose estimation in practical scenarios, addressing challenges like camera-object distance ratios and image noise [18]. This latter article proposes and qualifies a vision-based method for inner liner dynamic measurements. To this aim, relevant literature on small, planar target studies crucial for applications in constrained spaces, [19–23], is analysed. Finally, [24] proposes external parameter calibration methods and explore specific calibration motion models for their application.

The reason for such a deep understanding of the thermo-viscoelastic mechanisms, friction formation, and wear evolution—together with the growing demands of sustainability and vehicle electrification—is related to the development of predictive models and optimized materials that improve safety, efficiency, and environmental impact ([25]). The performance of a tire is strongly influenced by temperature, wear, inflation effects, and road-surface roughness, all of which govern rolling resistance, longitudinal stiffness, and the ability to generate reliable frictional forces ([26,27]). The aim of the presented work is the development of a completely new methodology to estimate the 6 degrees of freedom movement of a point of the inner liner, using a single commercial action camera mounted on the rim, balancing feasibility and efficiency. Utilizing a single camera fixed to the rim and a geometrically known target attached to the rigid body offers a novel approach to monitoring internal tyre surface movement. The selected action camera is a DJI 2, because of its low weight and small size. The developed system will be validated and studied on a flat track indoor machine available in the Pirelli Tyre S.p.A. testing department. This testing machine is used to study the dynamic behavior of the tire in controlled environmental conditions.

2. Proposed approach

A novel system was developed to measure and reconstruct the positions and orientations of a small target rigidly attached to the inner liner, using pose estimation with a single camera mounted on the rim. The system allows estimation of tyre dynamics by tracking a single reference point. The entire setup was designed from the ground up, incorporating an optimized and innovative camera support along with a customized pose estimation algorithm. Given the constraints of limited

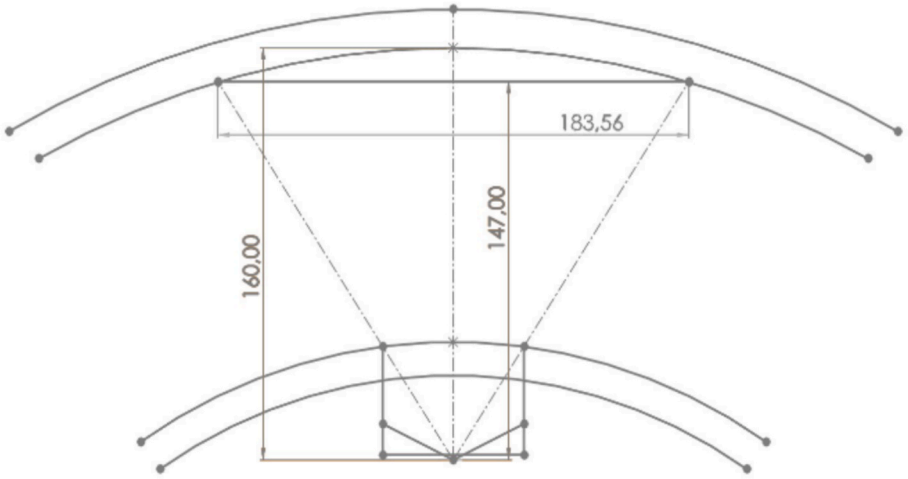

Fig. 3. Predicted field of view.

Fig. 4. Lightning system and camera support assembled on the rim.

Table 1
LEDs characteristics.

Dimension (mm)	Brightness (lm)	Forward voltage (V)	Color temp. (K)	Nominal power (W)
13.35x13.35	891	9	5000	6.3

space and weight considerations, a DJI Action 2 camera was selected. This camera allows to save data on a local microSD and a sufficient field of view (126°x71°). Furthermore, it can be controlled in real time via remote wireless connection. The experimental setup featured a 17″ wheel rim with a width of 7.5″, paired with a 225/55R17 Pirelli Cinturato™ ALL SEASON SF2 tyre.

2.1. System design

The initial concept for this system involved positioning a compact action camera within a metallic support, which was securely fastened to the wheel rim at a designated hole. This configuration allowed for an internal view of the tire. To ensure optimal performance, several critical factors were considered in the design of the system components.

First, a precise fit between the support and the rim was essential to guarantee both mechanical stability and pressure sealing. To achieve this, the rim's geometry was measured with 3D photogrammetry and subsequently replicated in CAD software to finally design the 3D camera support fitting the rim and the camera. As illustrated in Fig. 1, the geometry was specifically designed to be perpendicular to the rim surface, ensuring that the bolt holes aligned accordingly Fig. 2..

The second critical aspect concerns the radial dimension of the setup, as it significantly affects several key parameters. These include the distance between the camera and the target, the camera's radius of rotation (which is linked to the radial acceleration imposed to the camera during the revolution), the field of view (FOV), and potential

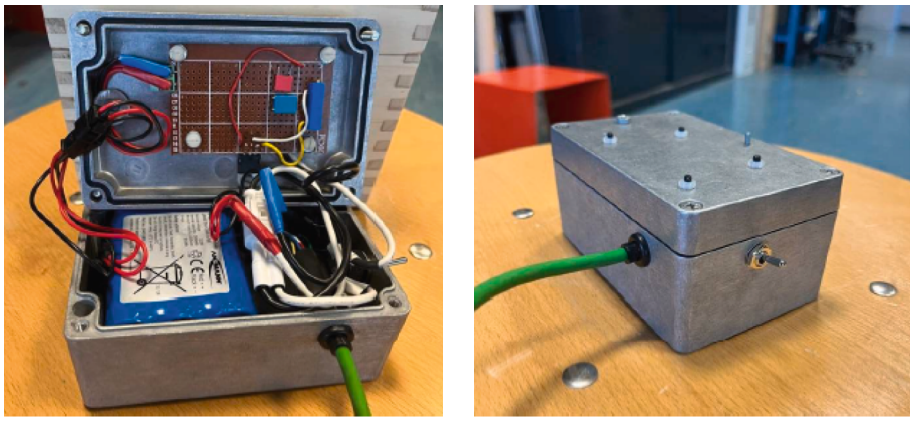

Fig. 5. Battery box: Internal view of the battery box (a), Outer view of the battery box (b).

Fig. 6. Scheme of the assembled system.

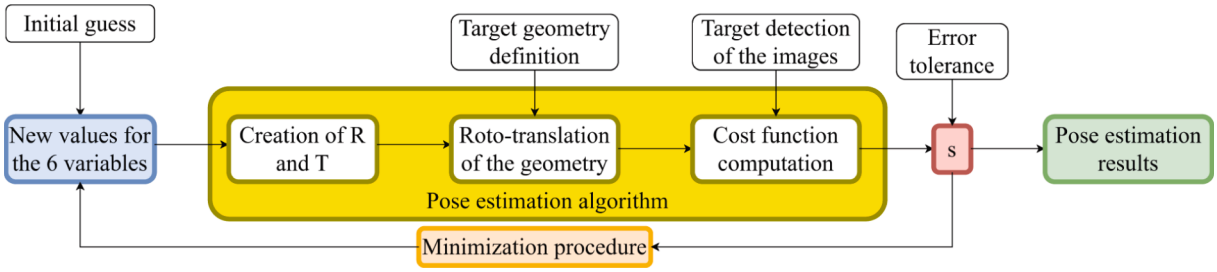

Fig. 7. Original algorithm.

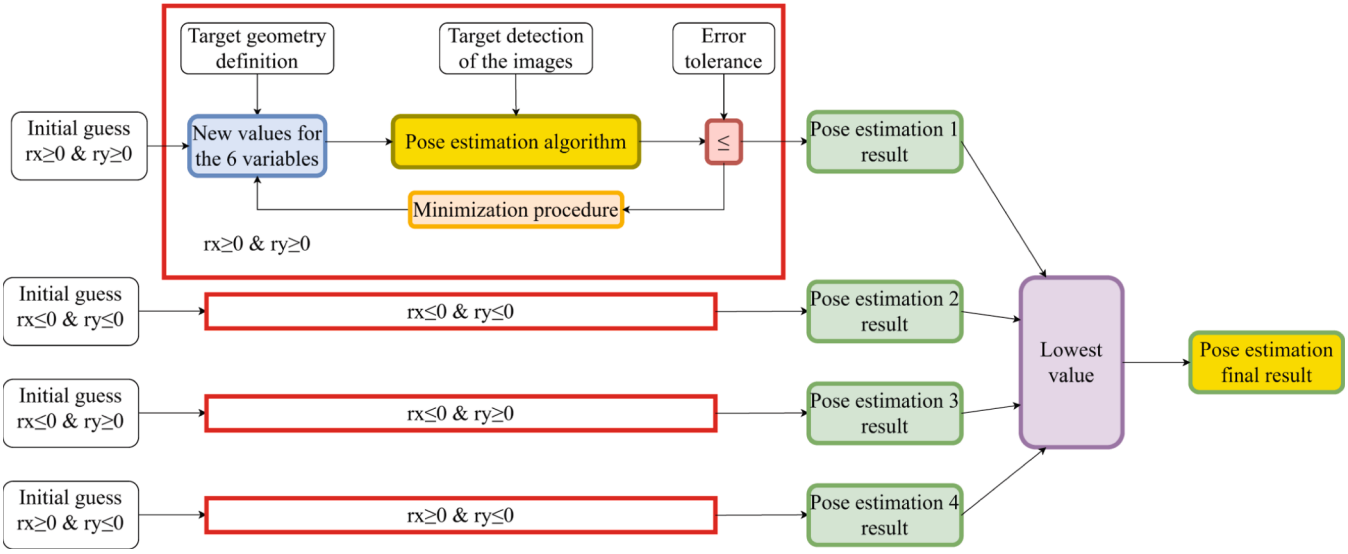

Fig. 8. Robust algorithm.

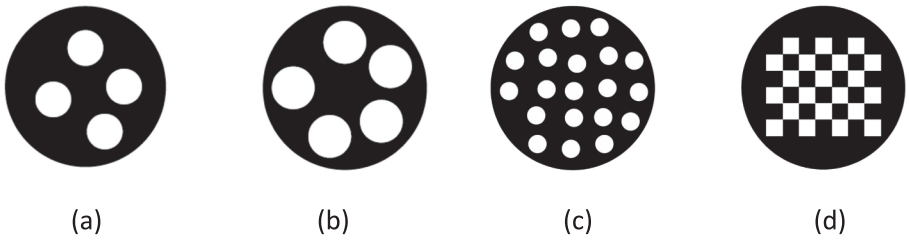

Fig. 9. Different types of tested targets.

Fig. 10. Experimental setup.

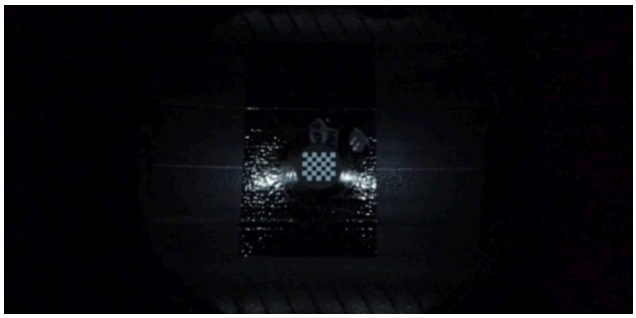

Fig. 11. Example of camera image.

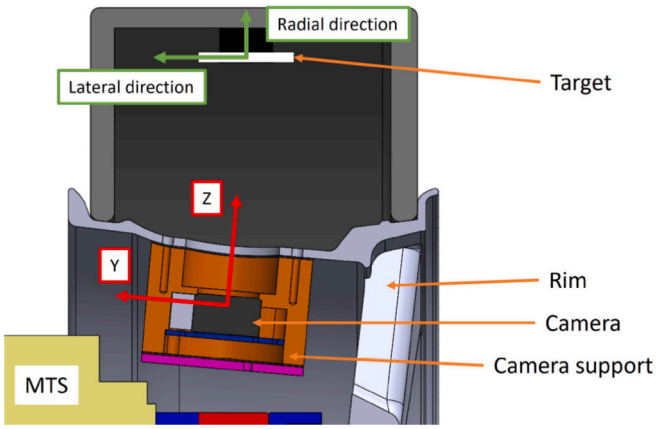

Fig. 12. Reference frame changing.

interferences between the camera support and the flat track setup.

The final dimensions of the support can be summarized as follows: an internal diameter of 55 mm and an external diameter of 95 mm. The number of bolts used to secure the system to the rim was limited to 6 × M5 to prevent excessive weakening of the rim structure. The support had a height of 62 mm, with a 5 mm thick cap, ensuring a minimum clearance of 13.3 mm between the support and the flat track setup.

At this stage, the support design was completed, leaving only the assessment of whether the camera, within this configuration, provided a sufficient field of view (FOV) to accurately observe the target inside the tire. This evaluation was conducted by creating a schematic representation of the entire system and measuring the dimensions of the tire area captured by the camera, as illustrated in Fig. 3. Given that the camera had a 126-degree viewing angle in wide video mode—sufficient to capture part of the support's side wall—the observed area of the tire had a nominal diameter of 18 mm. The final measured distance between the camera and the target was 147 mm.

To illuminate the target, two LEDs were installed at the two sides of the camera lens (Fig. 4). The diodes of the LEDs tent to show a change in temperature over a long period of utilization, which leads to a variable impedance and, in the end to a drift in the intensity of the emitted light. To prevent this issue, the LEDs were connected to an electronic circuit capable of producing constant current even when the impendence of the circuit was variable, ensuring that the emitted light was constant over time. The characteristics of the LEDs are summarized in the following table.

An exposure time of 1/6400 has been selected to ensure that the motion blur is negligible in this application. Moreover, the ISO parameter (6400) was chosen as the minimum to obtain a good brightness level with the given exposure time and lightning intensity provided by the LEDs (Table 1). The frame rate was 240, with 1080x1920. Fig. 4 shows the lightning system.

To ensure continuous operation of the camera during testing and to maintain illumination, a battery pack was mounted on the rim and rotate along with it. Consequently, a battery housing was designed, comprising two main components: fastening plates and the battery box. A larger, shock-resistant aluminum enclosure with an IP67-rated seal was selected to provide durability and protection. Additionally, an external switch was integrated to control the LEDs. The final component, incorporating these enhancements, is shown in Fig. 5.

Finally, in Fig. 6, the fully assembled setup can be observed. To compensate for the imbalance introduced by the camera support and battery box, these components were mounted opposite each other at a 180-degree angle.

2.2. Pose estimation algorithm

The pose estimation technique allows to estimate the 6dof of a rigid target of known geometry, providing that the camera calibration parameters are known. Camera calibration has been performed using the approach proposed by Zhang [28] in the camera calibration toolbox [29] developed by Bouguet [24], since it is open source tool and it allows a full control of the camera parameters. The pose estimation algorithm procedure can be divided into two main phases: the script creation and the target geometry definition.

2.3. Scripting development

The script was initially developed following the theory existing in

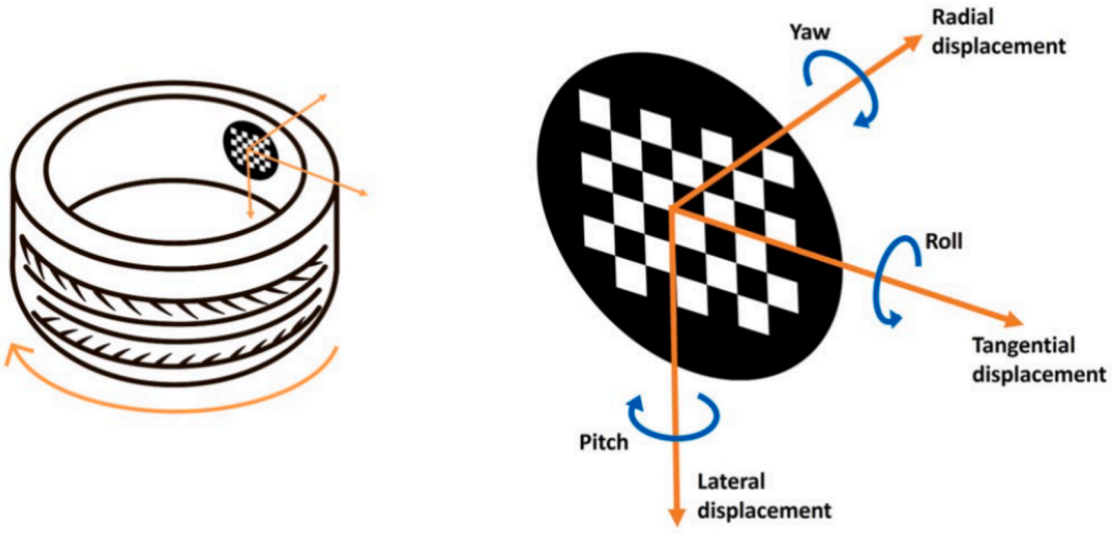

Fig. 13. Target reference frame and degrees of freedom.

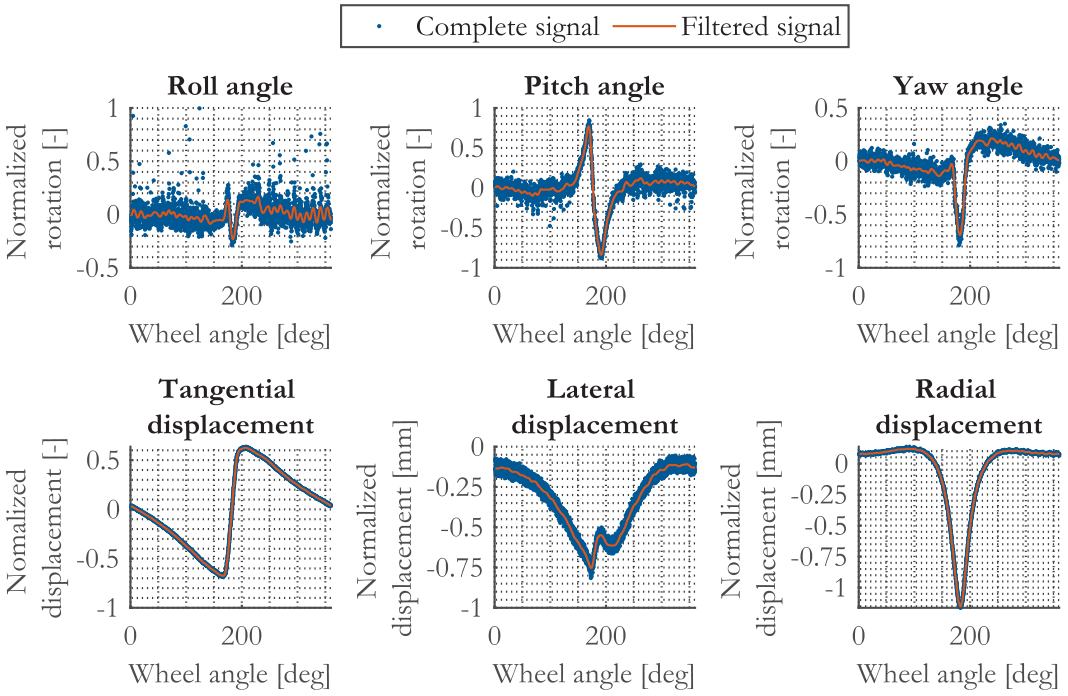

Fig. 14. Results from the data processing.

Table 2
Uncertainty related to the degrees of freedom.

	Roll Angle [°]	Pitch Angle [°]	Yaw Angle [°]	Tangential Displacement [mm]	Lateral Displacement [mm]	Radial Displacement [mm]
Reference Condition	0.85	0.59	0.04	0.06	0.06	0.10

literature [19] and the first implemented algorithm is schematized through the block diagram shown in Fig. 7, where R and T are the rotation and translation matrixes describing the roto-tranlsation between the target and the camera reference systems.

The main blocks of the diagram are:

- The values of the six variables, that are the 6 DOF that describe position and orientation of the target with respect to the camera.
- The roto-translation of the target geometry applied through Eq. (1):

$$P = RP_0 + T \tag{1}$$

- The cost function computation, which is the object space reprojection error [2] is computed by means of eq. (2):

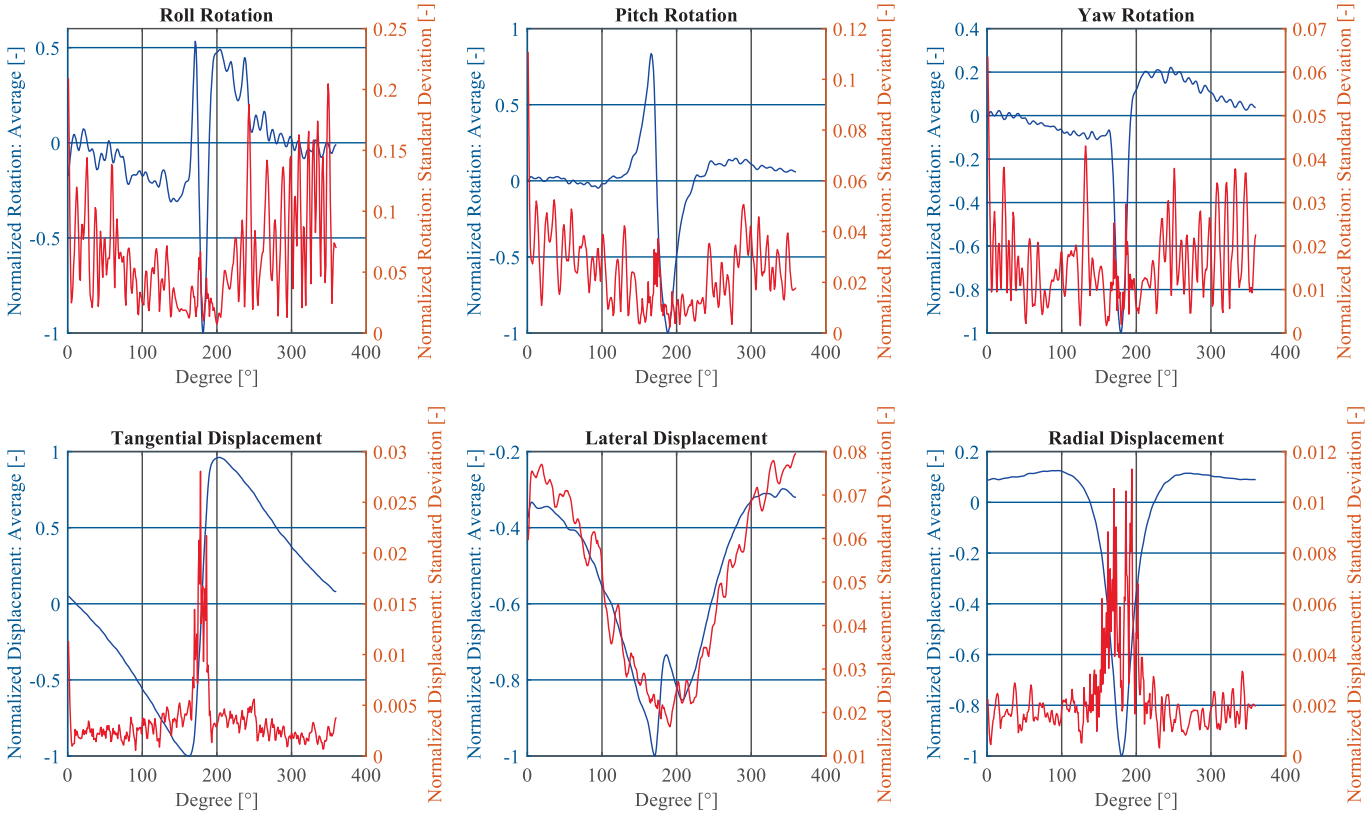

Fig. 15. Repeatability analysis on reference condition.

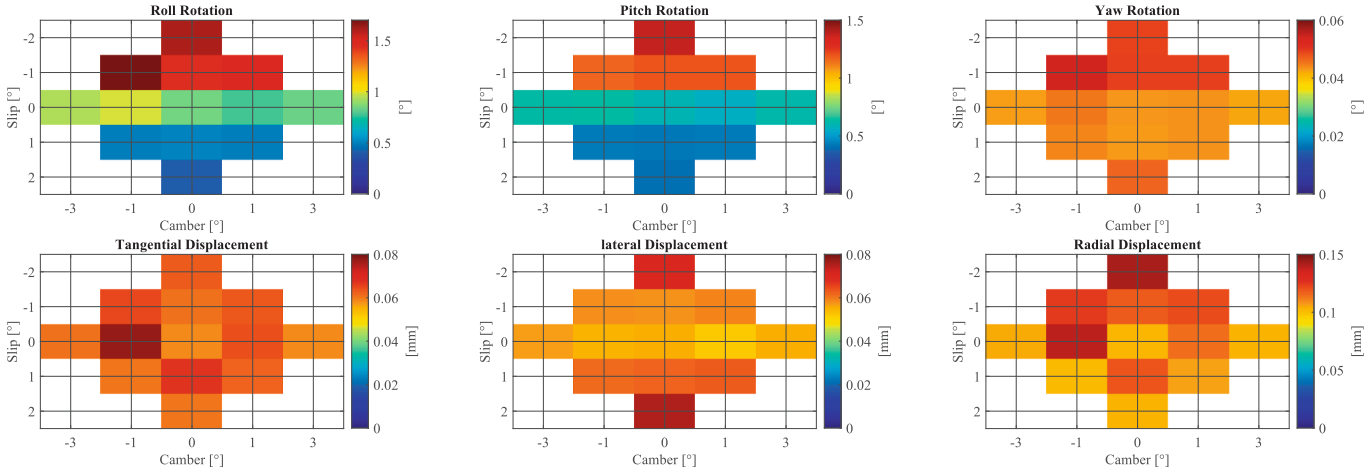

Fig. 16. Influence of camber and slip on the degrees of freedom of the rigid body.

$$E_{os} = \sum_{i=1}^{n} \left(\left\| (I - Q_i)\left(RP_0^i + T\right) \right\| \right)^2 \quad (2)$$

where $Q_i = (q_i q_i^T)/(q_i^T q_i)$ is the line-of sight projection matrix that, when applied to a scene point, projects the point orthogonally to the line of sight defined by the image point qi.

In order to find the minimum of constrained nonlinear multivariable cost functions, the interior-point algorithm [30] has been applied, as implemented in *fmincon* Matlab® function. The details of the optimization algorithm and the parameters of the optimization are out of the scope of this paper. However, the boundaries of the function were selected knowing that the target for this application couldn't physically move more than certain limits. For example, for the displacement along the radial direction of the tyre, it could not be bigger than 200 mm, indeed, the distance camera-target was expected to be around 150 mm. As optimization algorithm stopping criteria, the threshold on the first-order optimality measure [30] has been heuristically set to $1*10^{-10}$.

In some cases, eq (2) can have several local minima, and the iterative algorithm could converge toward one of these local minima instead of the global one leading to a wrong estimated pose. After several validation experiments, the algorithm was then implemented into a more robust version, capable of partially limiting the pose ambiguity [20]. The diagram representing the final version of the algorithm is shown in Fig. 8.

The idea behind this more robust algorithm was to divide the analysis into 4 independent cases; in each case the values of the two rotations

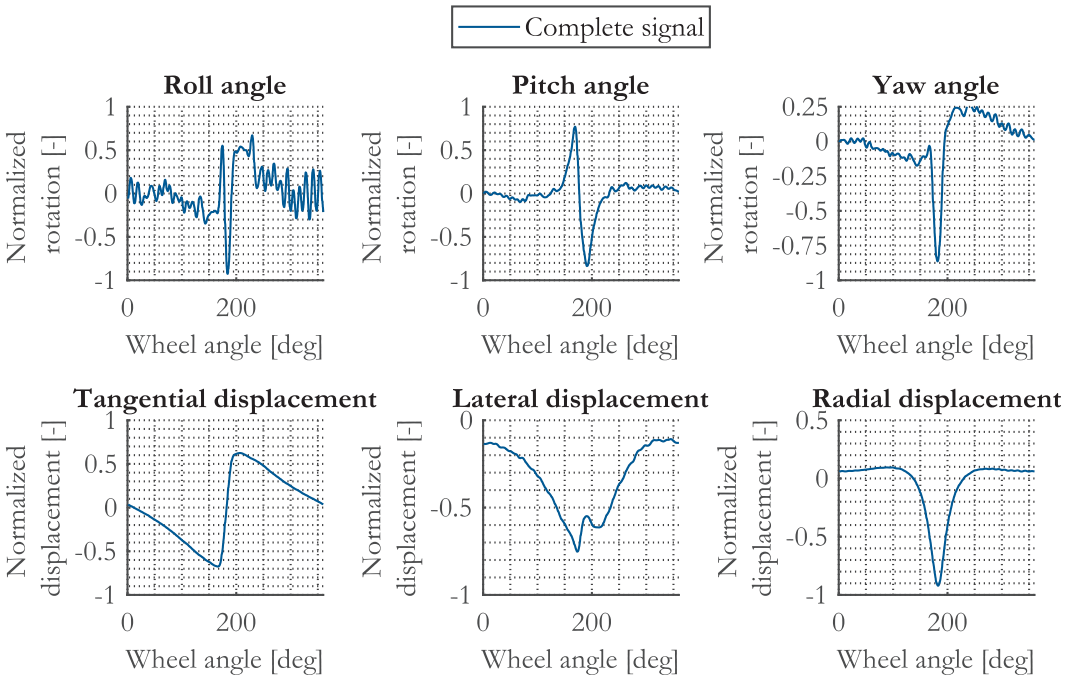

Fig. 17. Reference conditions. Camber and slip are fixed as null and vertical load is fixed at the load index.

rx and ry could only be either positive or negative. In this way, it was possible to consider up to 4 minimization scenarios. Each scenario leads to a pose estimation result, which correspond to a local minima. The global minima is the one associated to the lowest value of the cost function and therefore it was selected as the pose estimation final result.

2.4. Target geometry

The target geometry was designed to fit within a highly constrained space—specifically, the top of the rigid body—while also withstanding high accelerations without deforming or breaking. To meet these requirements, a planar target printed on paper was selected as the optimal solution. A first symmetric target composed of 4 holes has been tested. This configuration leads to large ambiguity in the reconstruction of the rotation around the axis exiting the plane of the target when the other two angles are null. If the target is parallel to the camera, the rotation around the axis exiting the plane is characterized by periodicity. Therefore, asymmetric design of the target is mandatory to quantify the rotation around each axis. Fig. 9 illustrates the various target design iterations considered during development.

Targets a and b were designed to investigate whether asymmetry could mitigate ambiguity. Nevertheless ambiguity persists, it is reduced to value close to zero. Target c was developed to increase the number of reference points and assess whether this could help eliminate ambiguity. Although the results showed significant improvement, some specific frames still exhibited ambiguity.

Target d was designed based on insights gained from previous tests. It was observed that introducing asymmetry alone did not resolve the ambiguity; however, increasing the number of reference points in the target geometry improved the results. Consequently, the checkerboard pattern shown in Fig. 9d was selected, offering two key advantages over white circular markers:

The reference points were the intersections between adjacent black and white squares, which could be precisely detected and extracted using a built-in MATLAB function. This method provided significantly higher accuracy compared to the blob analysis used for circular markers.

The checkerboard's regular pattern allowed for a substantial increase in the number of reference points, raising the total from a maximum of 20 (achieved with circular markers) to 30. This enhancement maximized the benefits of having a higher density of points to define the geometry.

Following the optimization process, the final target design was a 6 × 7 checkerboard pattern, with each square measuring 3 × 3 mm, as shown in Fig. 9d.

2.5. Experimental test

The experiment was performed at the testing department of Pirelli Tyre S.p.A., where the wheel was positioned onto a testing machine that reproduces the usage of a vehicle tyre, but under controlled conditions. The entire setup assembled onto the machine is shown in Fig. 10.

A total of 44 test conditions was considered, including all the different combinations of the imposed external parameters. In particular, the test with three levels of speeds, three levels of slip and camber and combination of the parameters. In this paper, examples of results are reported. The techniques allowed to successfully measure the six dof of the target and to successfully capture the different tyre behaviour. The image acquisition frame rate was 240 frames per second, while the image resolution was 1080x1920 px.

2.6. Data processing

The raw results of the experimental test are a series of videos, one for each condition, that had to be analysed to extract the information. An example of video frame is shown in Fig. 11.

At the end of the pose estimation analysis, the results are a set of 6 signals, one for each degree of freedom, describing the time history of the target displacements and rotations. To significantly improve these results and to make them usable, some other postprocessing steps had to be performed.

The first step was the reference frame changing [31]. This is done since it is necessary to align the results to the tire-fixed reference frame, shown in green in Fig. 12.

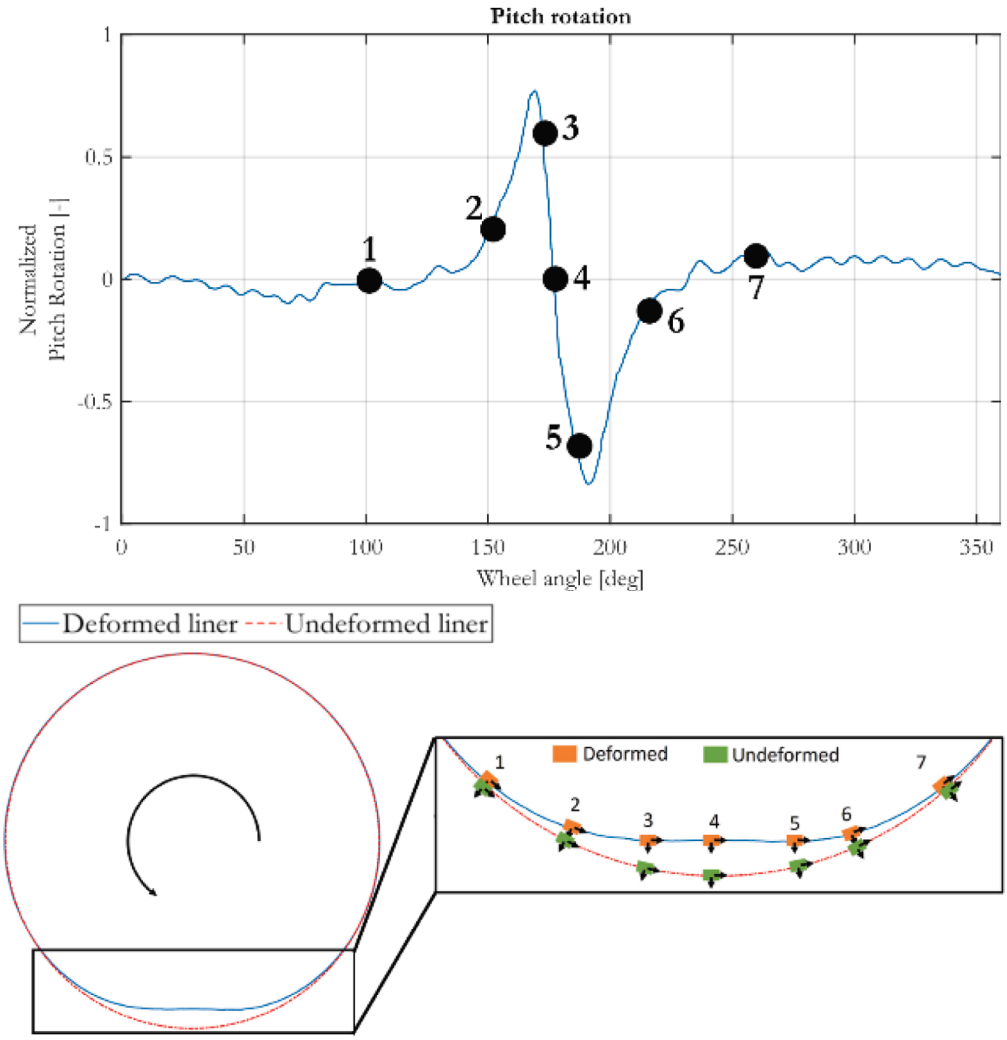

Fig. 18. Reference condition: pitch rotation (a) and physical explanation (b).

Since the maximum camera frame rate is 240 fps, depending to the wheel angular velocity, the samples per revolution can change, but for example at 40 km/h only 45 samples per revolution can be measured. Therefore, signals realignment into one wheel cycle was implemented, to go from a time history for each test of more than 100 wheel cycles at low resolution, to a single cycle with high resolution, by realigning all the cycle into one. Extracted signals are the rotations and displacements of the target. Thus, the target can be seen as a 3D object, thus composed by 6 degrees of freedom, described in Fig. 13..

Finally, the reconstructed signals were filtered, to remove the high frequency noise, not representative of physical target dynamics. An example of this final step is shown in Fig. 14, which illustrates the time histories of the target 6 degrees of freedom estimated through pose estimation. The signals representing the roll and pitch angles, as seen in the figure, exhibit a few points—outside the contact region—that are clearly outliers in relation to the general trend. This phenomenon is most likely due to high noise levels in the images corresponding to these points, which caused the pose estimation algorithm to converge on an incorrect pose of the target. However, this issue appears to be limited not only under the specific testing conditions presented here but also across all acquired signals. It can be easily mitigated when the mean trend is extracted.

To estimate the uncertainty linked to the estimation of the three rotations and three translations, the standard deviation of the discrepancies between the measured data (Fig. 14 blue points) and the smoothed lines (figure 14 red line) is shown in the Table 2..

Since angles are computed from displacement-derived quantities, their associated uncertainty is higher. However, to allow for a meaningful comparison, uncertainties are expressed as a fraction of the signal range (max–min) over a lap. According to this metric, angular uncertainty remains significantly lower than the maximum observed angle.

Moreover, the reference condition test has been repeated to confirm the repeatability of the data (Fig. 15.). The blue curve shows the mean trajectory computed over several repetitions, and the red curve represents the standard deviation among the different trials. Normalization, done to be compliant with a non-disclosure agreement, has been performed on the maximum value of the average to guarantee the correct comparison with the standard deviation.

For a deeper understanding of the influence of slip and camber on measuring uncertainty, Fig. 16. highlights the uncertainty associated with the different combination of slip and camber.

It can be observed that the most significant influence is associated with the slip angle, which also exhibits slightly higher measurement uncertainty. Notably, the highest absolute uncertainty is found in the radial displacement component, which corresponds to the direction with the largest overall displacement. This suggests that both the magnitude of the physical quantity and its sensitivity to operating conditions contribute to the observed uncertainty levels.

2.7. *Applicability of the technology and operational considerations*

The application of optical acquisition technologies in the analysis of

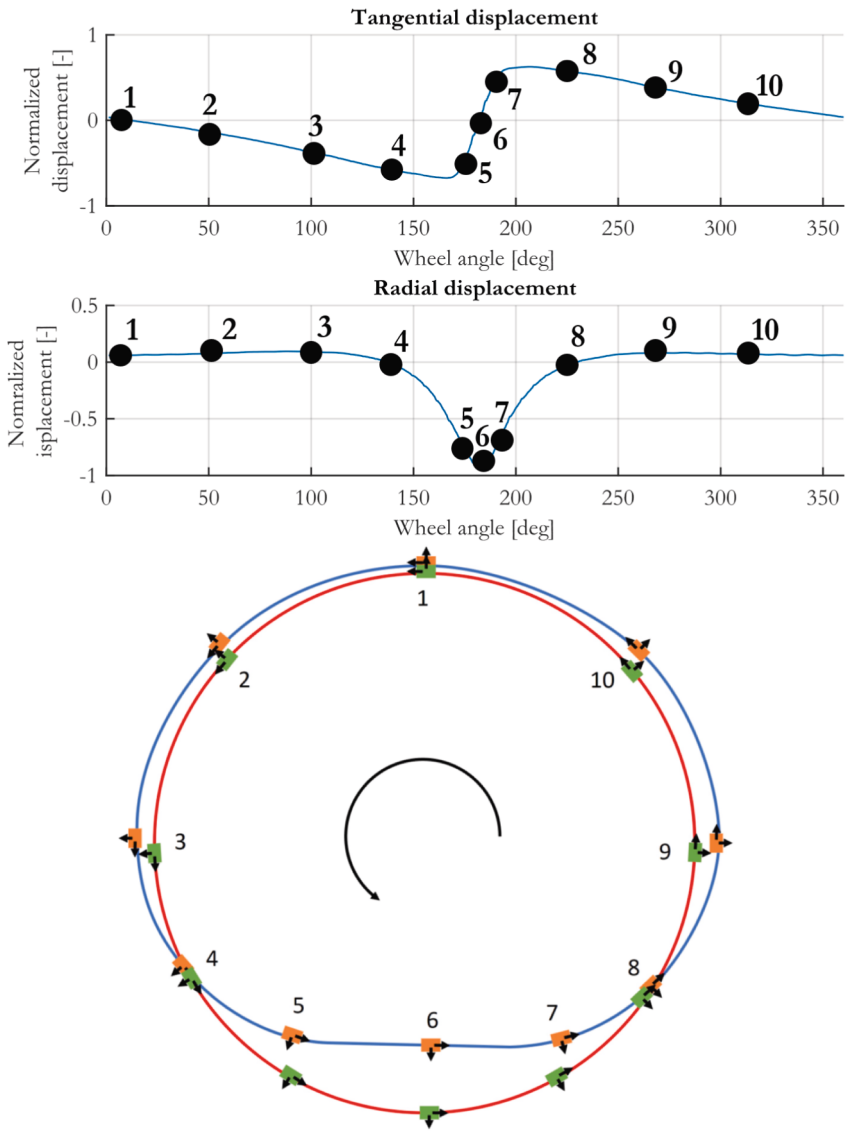

Fig. 19. Reference condition: tangential and radial displacements (a) and physical explanation (b).

tyre dynamics is significantly influenced by both geometric and dynamic parameters. One of the most critical factors is the sidewall height of the tyre. In the case of ultra-low-profile tyres, the reduced internal volume can limit the available space for sensor placement and for the camera focusing. To address these issues, the camera is mounted within a dedicated support structure affixed to the rim, positioned as close as possible to the tyre's rotational axis. This configuration ensures that the optical system remains sufficiently distant from the inner liner, thereby facilitating the focusing, minimizing image distortion and preserving acquisition fidelity.

As rotational speed increases, centrifugal forces become a dominant factor, potentially inducing deformation in the optical components and altering the perceived geometry of the target. The aforementioned support structure plays a crucial role in mitigating these effects by reducing the radial distance between the camera and the rotation axis. This design choice effectively lowers the inertial loads acting on the optical system, thereby enhancing its mechanical stability and operational reliability.

Higher rotational speeds also necessitate an increased sampling frequency to maintain adequate angular resolution. Under these conditions, the camera's exposure time must be reduced to prevent motion blur, which in turn requires enhanced illumination to ensure sufficient image quality. To further improve angular resolution and accurately capture the dynamic behaviour of the tyre, it is often advantageous to concatenate data acquired over multiple revolutions. This approach leverages synchronization and temporal averaging techniques to enhance measurement robustness.

Several practical constraints must be considered when implementing this technology:

- Maximum rotational speed: Beyond a certain threshold, the quality of optical acquisition may degrade due to mechanical and optical limitations.
- Centrifugal deformation of optical components: If not properly compensated, these effects can compromise measurement accuracy.

Importantly, the integration of a single camera mounted on the rim has been shown not to interfere with the tyre's dynamic behaviour. This non-intrusive configuration enables precise observation of the inner liner's motion under real operating conditions.

These considerations must be carefully balanced in the design and deployment of the measurement system to ensure the reliability, repeatability, and accuracy of the data collected during experimental testing.

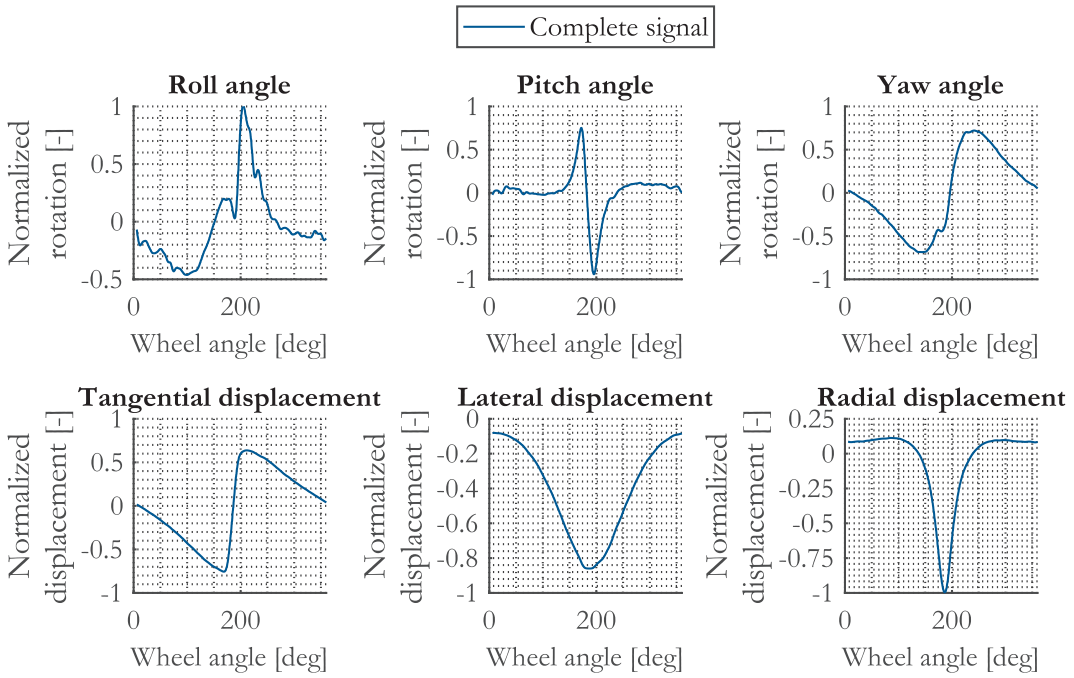

Fig. 20. Negative slip angle results.

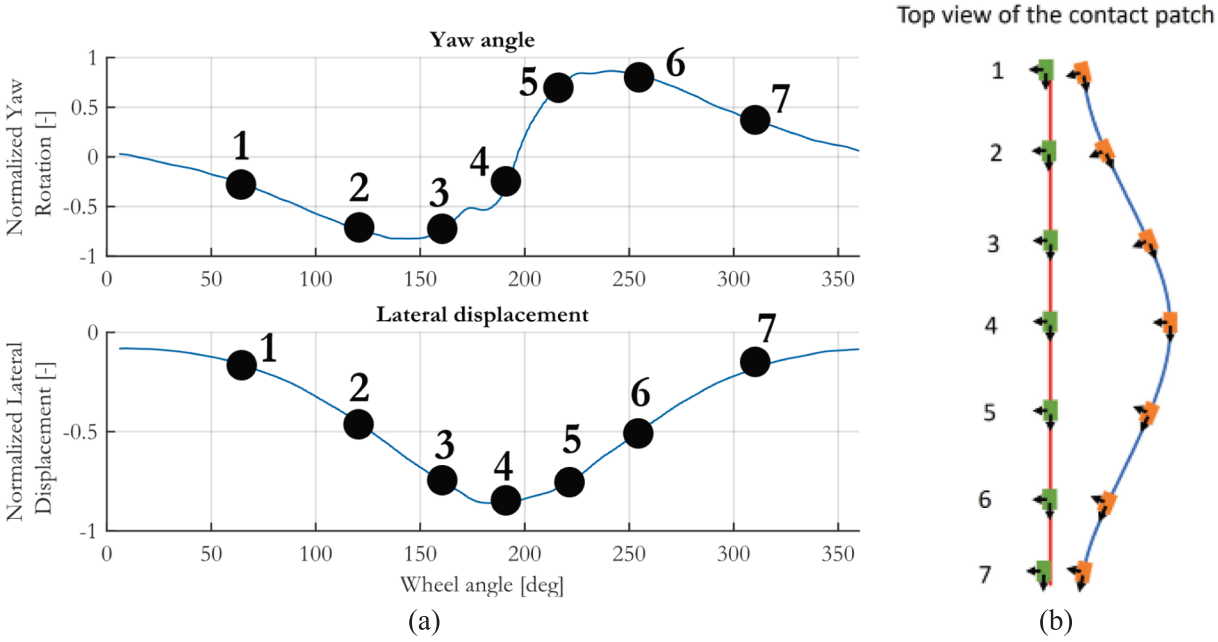

Fig. 21. Slip angle non-null: yaw angle and lateral displacement (a), physical explanation (b).

2.8. Results

The final outputs of the pose estimation application are the estimated values of the target's six degrees of freedom in each testing condition and for one wheel revolution.

2.9. Reference condition

Fig. 17 highlights results for the reference condition case, for which slip angle and camber angle are null, and the vertical load is fixed at load index.

All the displayed values correspond to rotations or displacements relative to the reference condition, with the contact region positioned at half of the wheel's rotation. For instance, in the case of radial displacement, it can be observed that the target moved in the negative direction (i.e., toward the centre of the wheel) relative to the reference condition.

Among the six signals, the roll angle appears to be the noisiest; however, during the contact region, it is well-defined.

The pitch angle exhibits the largest amplitude among the rotational signals, primarily due to the movement of the target through the contact patch. This region can be considered a flat section of the undeformed circumference. As the target moves along this section, its dynamics are measured as a positive rotation at the entrance and a negative rotation at the exit. A graphical representation of this phenomenon is shown in

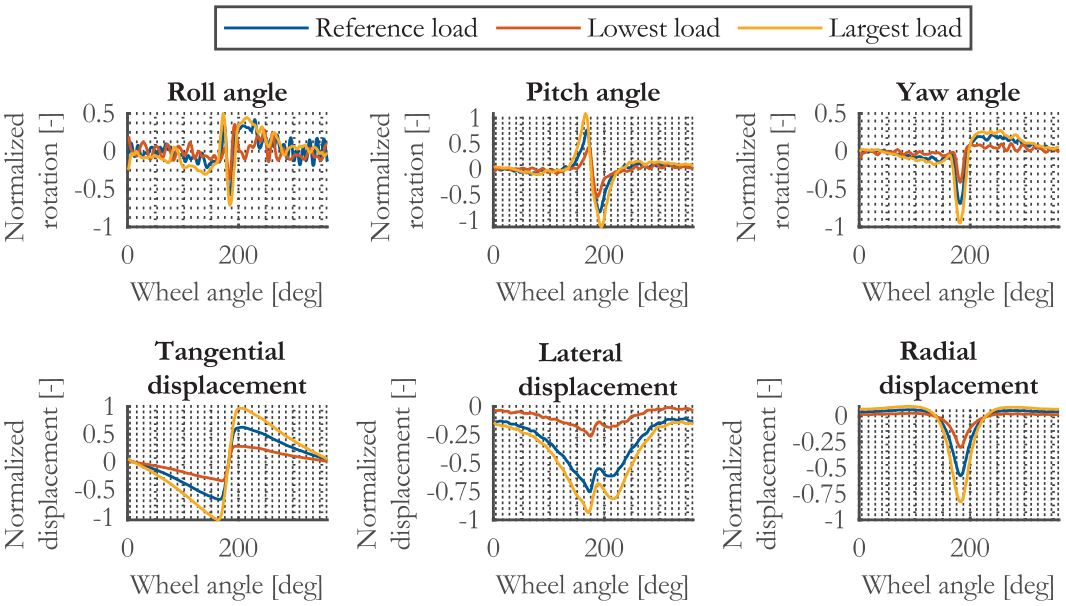

Fig. 22. Sensitivity with respect to the vertical load.

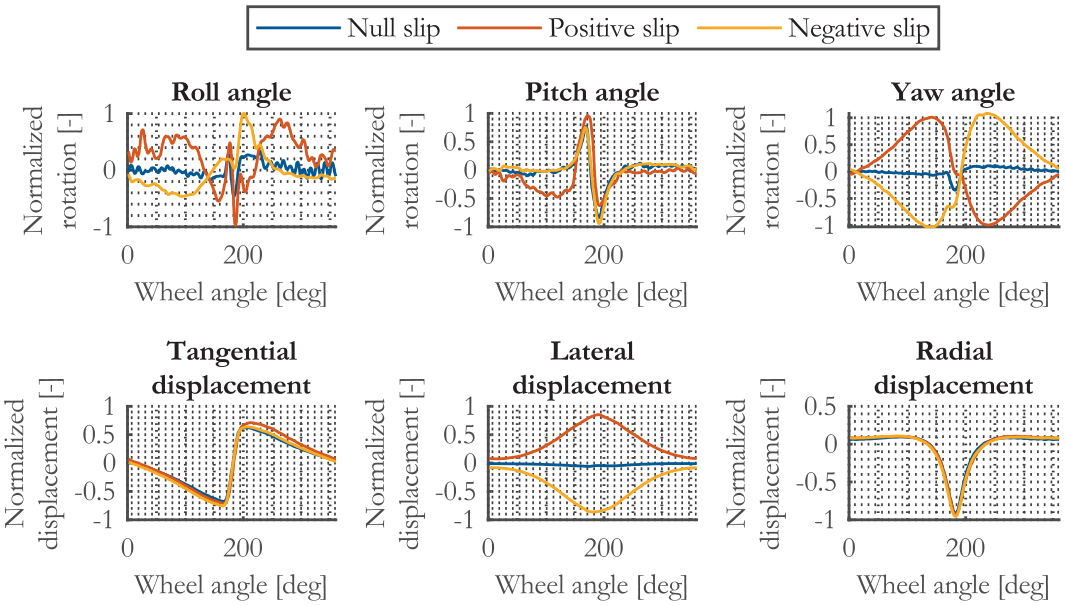

Fig. 23. Sensitivity with respect to the slip angle.

Fig. 18.

Furthermore, always with reference to Fig. 18, the yaw angle, being different from zero, is an expected behaviour linked to the phenomena of conicity and ply steer—two tire characteristics caused by the asymmetry of its structure. During tire production, various configurations can be used to construct the tire body, primarily by altering the directions of the plies. This asymmetry can result in deviations in the tire's behaviour, even when traveling straight.

The lateral displacement exhibits a small deviation from zero for the same reasons that explain the yaw angle. Due to structural asymmetry, the tire moves slightly sideways even when traveling straight.

Tangential and radial displacements are the most straightforward signals to interpret. Both are generated by the movement of the target along a deformed circumference, which is larger than the undeformed circumference outside the contact patch and smaller inside it. This phenomenon is illustrated in Fig. 19, where the deformed liner is exaggerated to better highlight the target's movements.

2.10. Slip angle

Interesting condition to analyse regards when the slip angle is different than zero (Fig. 20.).

The interesting signals in this case are yaw angle and lateral displacement, being the two more affected by the presence of a slip angle. A scheme representing the contact path in deformed and undeformed configurations is displayed in Fig. 21..

From the above figure it is possible to see that the liner tends to deform significantly toward in the lateral direction, and when the target is approaching the contact region it will move consequently in that direction as well as rotating around the z-axis and producing the rotations displayed by the yaw angle graph.

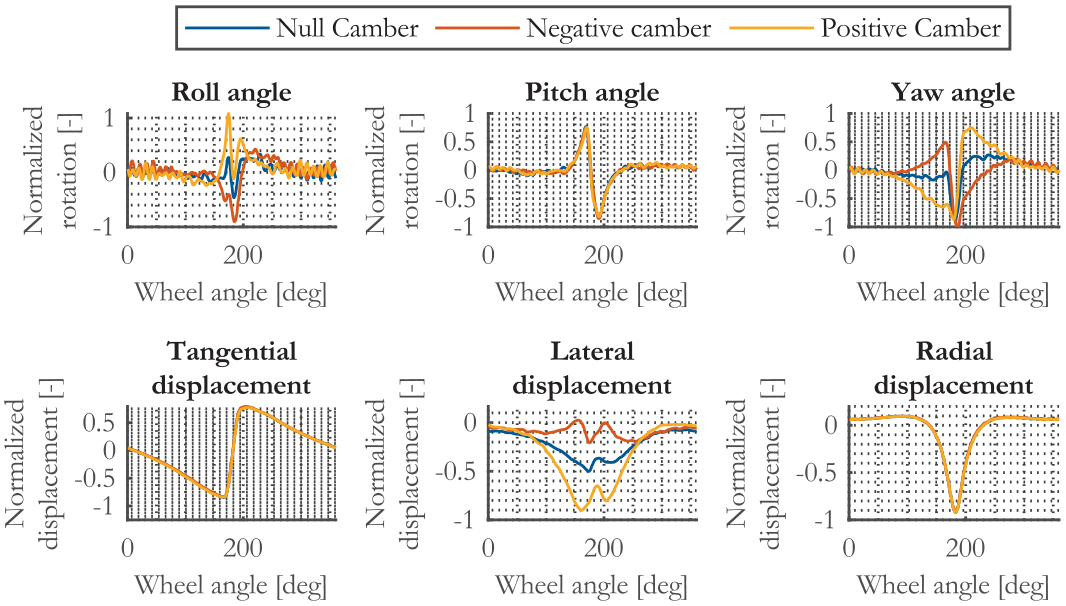

Fig. 24. Sensitivity with respect to the camber angle.

2.11. *Parameters sensitivity*

To understand the goodness of the measurement techniques, it is possible to compare different testing condition.

As a first case, Fig. 22. reports the sensitivity with respect to the vertical load.

It is interesting to notice that the noise level is lower than the different behaviour in the three conditions. Same interesting results can be achieved even changing slip angle (Fig. 23.) or giving a different camber angle (Fig. 24.). Both cases show that the signal noise is lower than the different behaviour of the three conditions.

3. Conclusions

This study presented the development and validation of a non-intrusive optical measurement system for tracking the motion of a rigid body mounted on the inner liner of a rotating tyre. The system relies on a single camera installed on the rim, supported by a dedicated structure designed to minimize centrifugal loads and maximize available space. This configuration was shown not to interfere with the tyre's dynamic behaviour, enabling accurate and repeatable measurements under real operating conditions.

The proposed technique successfully captured the six degrees of freedom of the target and was validated through a comprehensive test campaign involving multiple combinations of speed, slip, and camber. The results demonstrated the system's ability to detect and distinguish different tyre behaviours, offering valuable insights into tyre dynamics.

Uncertainty analysis revealed that angular measurements, derived from displacement data, exhibit higher absolute uncertainty. However, when normalized by the signal range over a lap, angular uncertainty remained significantly lower than the maximum observed angle. Repeatability was confirmed through repeated tests under reference conditions, with the mean trajectory and standard deviation illustrating the system's consistency.

The methodology enabled the generation of a substantial volume of 3D data, providing an accurate description of the tyre's single-point dynamics with low uncertainty across most conditions. The extensive range of operational parameters tested yielded a large set of comparable results. In particular, the analysis of a single target's motion allowed for a direct comparison of the effects of camber, slip, and their combination on tyre behaviour. Additionally, the influence of vertical load, inflation pressure, and speed on tyre dynamics was thoroughly investigated.

The proposed method is generally adaptable to different tyre sizes and profiles, although its performance depends on geometric compatibility with the camera's characteristics. Future hardware improvements, such as more compact systems and faster acquisition, will further extend applicability across a wider range of tyre geometries and operating conditions. Lastly, the methodology was validated under standard operating conditions, including nominal inflation pressures and typical test speeds, where significant variations are not expected. Temperature effects and tyre wear appear negligible within the tested range, although temperature influence remains to be explicitly validated. For real-road applications, similar performance is anticipated under comparable speeds, with potential deviations only in cases of abrupt accelerations or highly irregular surfaces, which represent areas for future investigation.

Overall, the proposed approach offers a robust and versatile tool for experimental investigations and model validation in vehicle dynamics research.

CRediT authorship contribution statement

Emanuele Zappa: Writing – review & editing, Writing – original draft, Validation, Supervision, Resources, Methodology, Formal analysis, Data curation, Conceptualization. **Luca Parenzan:** Software, Resources, Formal analysis, Data curation. **Edoardo Montini:** Writing – review & editing, Writing – original draft, Supervision, Resources, Methodology, Investigation, Formal analysis, Data curation, Conceptualization. **Stefano Melzi:** Supervision, Project administration, Conceptualization. **Andrea Gregorini:** Supervision, Software, Resources, Methodology, Data curation, Conceptualization. **Andrea Natta:** Writing – review & editing, Supervision, Project administration.

Declaration of competing interest

The authors declare that they have no known competing financial interests or personal relationships that could have appeared to influence the work reported in this paper.

Acknowledgement

We would like to thank Pirelli Tyre S.p.A., particularly the Cyber and Indoor testing department, for the opportunity and support in carrying

out this research activity. Their contribution was essential to the success of our study.

Data availability

The data that has been used is confidential.

References

[1] M.B. Yilmazoglu, J. Sigmund, E. Genc, H.L. Hartnagel, Integrated inas/gasb 3d magnetic field sensors for "the intelligent tire", Sens. Actuators, A 94 (1) (2001) 59–63.

[2] A.J. Tuononen, L. Hartikainen, Optical position detection sensor to measure tyre carcass deflections in aquaplaning, Veh. Syst. Dyn. 46 (6) (Jan 2008) 471–481.

[3] Ari J Tuononen. Laser triangulation to measure the carcass deflections of a rolling tire. Measurement Science and Technology, 22(12):125304, nov 2011.

[4] Kanwar Bharat Singh and Saied Taheri. Accelerometer based method for tire load and slip angle estimation. Vibration, 2(2):174–186, apr 2019.

[5] E. Zappa, L. Parenzan, E. Montini, S. Melzi, A. Gregorini and A. Natta, "Measurement of the Dynamics of a Tire's Inner Liner With Digital Image Correlation," in IEEE Transactions on Instrumentation and Measurement, vol. 74, pp. 1-10, 2025, Art no. 4509510, doi: 10.1109/TIM.2025.3566849.

[6] H. Dong et al., "Liquid Metal-Based Flexible Sensing and Wireless Charging System for Smart Tire Strain Monitoring," in IEEE Sensors Journal, vol. 24, no. 2, pp. 1304-1312, 15 Jan.15, 2024, doi: 10.1109/JSEN.2023.3339978.

[7] H. Wu, X. Wang, D. Lu, Tire force estimation using intelligent tire system detecting carcass deformation, SAE Technical Papers (2024), https://doi.org/10.4271/2024-01-2293.

[8] R.G. Cestari, A. Lucchini, E. Leati, M. Norgia, S. Formentin, S.M. Savaresi, Vertical load estimation in tractors via in-wheel optical sensing, IFAC-PapersOnLine, Volume 58, Issue 15, 2024, Pages 532-537, ISSN 2405-8963.

[9] Xueliang Gao, Yi Xiong, Weiping Liu, Ye Zhuang, Modeling and experimental study of tire deformation characteristics under high-speed rolling condition, Polymer Testing, Volume 99, 2021, 107052, ISSN 0142-9418.

[10] Filip Feldesi, Theunis R. Botha, P. Schalk Els, Full-field strain measurements of the inside of an agricultural tyre using digital image correlation, Journal of Terramechanics, Volume 91, 2020, Pages 309-318, ISSN 0022-4898.

[11] Liu, Z., Guan, B., Shang, Y., Bian, Y., Sun, P., Yu, Q. Stereo Event-Based, 6-DOF Pose Tracking for Uncooperative Spacecraft (2025) IEEE Transactions on Geoscience and Remote Sensing, 63, art. no. 5607513, .

[12] B. Guan, J. Zhao, D. Barath, et al., Minimal solvers for relative pose estimation of multi-camera systems using affine correspondences, Int. J. Comput. Vis. 131 (2023) 324–345, https://doi.org/10.1007/s11263-022-01690-w.

[13] Kuai Zhou, Xiang Huang, Shuanggao Li, Hangyu Li, Shengjie Kong, 6-D pose estimation method for large gear structure assembly using monocular vision, Measurement, Volume 183, 2021, 109854, ISSN 0263-2241, https://doi.org/10.1016/j.measurement.2021.109854.

[14] Yuansheng Cheng, Zhe Tian, Donghong Ning, Ke Feng, Zhixiong Li, Sumika Chauhan, Govind Vashishtha, Computer vision-based non-contact struttura vibration measurement: Methods, challenges and opportunities,Measurement, Volume 243, 2025, 116426, ISSN 0263-2241, https://doi.org/10.1016/j.measurement.2024.116426.

[15] M.A. Fischler, R.C. Bolles, Random sample consensus: a paradigm for model fitting with applications to image analysis and automated cartography, Commun. ACM 24 (6) (1981) 381–395.

[16] D. Oberkampf, D.F. DeMenthon, L.S. Davis, Iterative pose estimation using coplanar feature points, Comput. Vis. Image Underst. 63 (3) (1996) 495–511.

[17] K. Zhou, X. Wang, Z. Wang, H. Wei, L. Yin, Complete initial solutions for iterative pose estimation from planar objects, IEEE Access 6 (2018) 22257–22266.

[18] C.-P. Lu, G.D. Hager, E. Mjolsness, Fast and globally convergent pose estimation from video images, IEEE Trans. Pattern Anal. Mach. Intell. 22 (6) (2000) 610–622.

[19] Yi Ma, Stefano Soatto, Jana Kosecka, and S. Shankar Sastry. An Invitation to 3-D Vision: From Images to Geometric Models. SpringerVerlag, 2003.

[20] Richard Hartley and Andrew Zisserman. Multiple View Geometry in Computer Vision. Cambridge University Press, 2 edition, 2004.

[21] Bernd Jahne. Practical Handbook on Image Processing for Scientific and Technical Applications. CRC Press, 2 edition, 2004.

[22] J. Heikkila and O. Silven. A four-step camera calibration procedure with implicit image correction. In Proceedings of IEEE Computer Society Conference on Computer Vision and Pattern Recognition, pages 1106–1112, 1997. 142 | Bibliography.

[23] Zhengyou Zhang. Flexible camera calibration by viewing a plane from unknown orientations. In Proceedings of the Seventh IEEE International Conference on Computer Vision, volume 1, pages 666–673, 1999.

[24] Z. Liu, S. Liang, B. Guan, D. Tan, Y. Shang, Q. Yu, Collimator-assisted high-precision calibration method for event cameras, Opt. Lett. 50 (13) (2025) 4254–4257, https://doi.org/10.1364/OL.564294.

[25] Fathi, H., El-Sayegh, Z., Ren, J. Temperature-Dependent Analysis of the Tire-Road Interaction Characteristics for a Passenger Car Tire Using Finite Element Analysis, (2025), SAE International Journal of Passenger Vehicle Systems, 18 (2). DOI: 10.4271/15-18-02-0010.

[26] Sakhnevych, A., Genovese, A. Tyre wear model: A fusion of rubber viscoelasticity, road roughness, and thermodynamic state, (2024), Wear, 542-543, art. no. 205291. DOI: 10.1016/j.wear.2024.205291.

[27] Soica, A., Gheorghe, C. Tire–Road Interaction: A Comprehensive Review of Friction Mechanisms, Influencing Factors, and Future Challenges, (2025), Machines, 13 (11), art. no. 1005. DOI: 10.3390/machines13111005.

[28] Jean-Yves Bouguet. Camera calibration toolbox for matlab. CaltechDATA, May 2022.

[29] Jean-Yves Bouguet. Camera calibration toolbox for matlab. CaltechDATA, May 2022.

[30] R.A. Waltz, J.L. Morales, J. Nocedal, D. Orban, An interior algorithm for nonlinear optimization that combines line search and trust region steps, Math. Program. 107 (3) (2006) 391–408.

[31] G. Schweighofer, A. Pinz, Robust pose estimation from a planar target, IEEE Trans. Pattern Anal. Mach. Intell. 28 (12) (2006) 2024–2030.